

# First Wind Tunnel Data of CALLISTO Reusable VTVL Launcher First Stage Demonstrator

Ansgar Marwege<sup>1</sup> Johannes Rieher<sup>2</sup> Josef Klevanski<sup>3</sup> Ali Gülhan<sup>4</sup>  
Tobias Ecker<sup>5</sup> Bodo Reimann<sup>6</sup> Etienne Dumont<sup>7</sup>

<sup>1</sup>*DLR, Institute of Aerodynamics and Flow Technology, Supersonic and Hypersonic Technologies Department, Linder Hoehe, 51147 Cologne, Germany, Ansgar.Marwege@dlr.de*

<sup>2</sup>*DLR, Institute of Aerodynamics and Flow Technology, Supersonic and Hypersonic Technologies Department, Linder Hoehe, 51147 Cologne, Germany, Johannes.Rieher@dlr.de*

<sup>3</sup>*DLR, Institute of Aerodynamics and Flow Technology, Supersonic and Hypersonic Technologies Department, Linder Hoehe, 51147 Cologne, Germany, Josef.Klevanski@dlr.de*

<sup>4</sup>*DLR, Institute of Aerodynamics and Flow Technology, Supersonic and Hypersonic Technologies Department, Linder Hoehe, 51147 Cologne, Germany, Ali.Guelhan@dlr.de*

<sup>5</sup>*DLR, Institute of Aerodynamics and Flow Technology, Spacecraft Department, Bunsenstr. 10, 37073 Göttingen, Germany, Tobias.Ecker@dlr.de*

<sup>6</sup>*DLR, Institute of Aerodynamics and Flow Technology, Spacecraft Department, Lilienthalplatz 7, 38108, Brunswick, Germany, Bodo.Reimann@dlr.de*

<sup>7</sup>*DLR, Institute of Space Systems, Robert Hooke-Str. 7, 28359 Bremen, German, Etienne.Dumont@dlr.de*

## Abstract

CALLISTO is a demonstrator for a reusable VTVL rocket. It is developed and built by DLR, JAXA, and CNES. The aerodynamics and aerothermodynamics of the vehicle are investigated at DLR. Experiments were performed in the Trisonic Wind Tunnel (TMK) at the Supersonic- and Hypersonic Flow Technologies Department in Cologne for Mach numbers between 0.5 and 2.5.

The experiments considered the ascent and decent configurations of the vehicle. This paper describes the tested configurations and the experimental methods. A comparison between the Aerodynamic Data Base, based on CFD, and the experimental results showed good agreement of the global coefficients.

## 1. Introduction

In order to make access to space more affordable for both scientific and commercial activities the German Aerospace Center (DLR), the Japanese Aerospace Exploration Agency (JAXA), and the French National Centre for Space Studies (CNES) joined in a trilateral agreement to develop and demonstrate the technologies that will be needed for future reusable launch vehicles. In the joined project CALLISTO (Cooperative Action Leading to Launcher Innovation in Stage Toss back Operations) a demonstrator for a reusable Vertical Take-off, Vertical Landing (VTVL) rocket, acting as first stage, is developed and built. As long-term objective this project aims at paving the way to develop a rocket that can be reused, and the joint efforts of the three agencies will culminate in a demonstrator that will perform its first flights from the Kourou Space Center in French Guyana. [3][4]

The aerodynamic and aerothermal behavior of the CALLISTO vehicle are investigated at DLR, including its challenging configurations with high angles of attack and subsonic up to supersonic flight regimes. To cross-check the aerodynamic data from CFD and for the enhancement of the understanding of the aerodynamic characteristics of the vehicle, experiments were performed in the Trisonic Wind Tunnel (TMK) at the DLR Department of Supersonic- and Hypersonic Flow Technologies in Cologne for Mach numbers between 0.5 and 2.5.

The experiments considered the ascent and the backwards orientated decent configurations of the vehicle with folded and deployed control surfaces. The angle of attack was continuously varied for all configurations. A comparison between the Aerodynamic Data Base (AEDB), based on Reynolds-Averaged Navier–Stokes (RANS) Computational Fluid Dynamics (CFD), and the experimental results showed good agreement and no significant deviations in the global coefficients were found.

This paper describes the tested configurations and the experimental methods of the test campaign. Furthermore, results for the ascent configuration and the descent configuration without thrust and with 0° deflection angle of the aerodynamic control surfaces are presented. An uncertainty analysis was performed for the experimental setup and the validity of the data was checked by comparison with data from CFD simulations performed with the DLR flow solver TAU. Follow-up papers will present the influence of the deflection angle of the fins on the aerodynamics of the vehicle [8][9] and evaluate the influence of the exhaust plume.

## 2. Trisonic Wind Tunnel TMK at DLR Cologne

The experiments presented in this paper were carried out in the Trisonic Wind Tunnel (TMK) at the DLR in Cologne. The TMK is a blow down wind tunnel with a Mach number range of  $0.5 < Ma < 5.7$ , and with a rectangular  $0.6 \text{ m} \times 0.6 \text{ m}$  test section. It is sketched in Figure 1. Compressed air from a pressure reservoir passes a storage heater, a settling chamber, a Laval nozzle, a test section and a diffuser. With the volume of the pressure reservoir of  $1000 \text{ m}^3$  at pressure of up to 60 bar, test durations of up to 60 seconds can be reached. During supersonic tests, the Mach number is controlled via the adaptable nozzle; for the transonic and subsonic regime it is controlled with the diffuser. The wind tunnel model is fixed in the test section on a motion control device, with which the incident angle of the model can be controlled. Due to the adaptable nozzle and the motion control device,  $\alpha$ -polars can be run for several Mach numbers in one run. In the transonic and subsonic regime, only one Mach number per run can be tested.

The wind tunnel is operated at a static pressure of  $p_\infty \approx 1 \text{ bar}$  for Mach numbers  $Ma < 1.2$ , and at a constant dynamic pressure  $q_\infty \approx 1 \text{ bar}$  for higher Mach numbers ( $Ma > 1.2$ ). Up to Mach 5.7 can be reached by heating the air in the storage heater and by the use of an ejector downstream of the diffuser. Due to the constant static pressure for  $Ma < 1.2$ , the dynamic pressure and, hence, the Reynolds number increases with increasing Mach numbers. The Reynolds numbers in this regime range from  $Re = 1.2 \times 10^7 \text{ m}^{-1}$  ( $Ma = 0.5$ ) to  $Re = 3.7 \times 10^7 \text{ m}^{-1}$  ( $Ma = 1.2$ ). For supersonic conditions, the Reynolds number can be varied in a range of  $2.6 \times 10^7 \text{ m}^{-1} < Re < 7.6 \times 10^7 \text{ m}^{-1}$  by variation of the stagnation pressure (up to  $p_0 = 25 \text{ bar}$ ) and temperature (up to  $T_0 = 550 \text{ K}$ ). The Reynolds number variation can be extended by the use of the ejector.

For transonic and subsonic tests a test section with perforated walls is installed downstream of the supersonic test section. By variation of the aperture of the perforations, the boundary layer suction can be adapted to the flow conditions. The supersonic test section is equipped with large glass windows, which allow for investigations with schlieren technique in the supersonic regime. Due to the perforated walls installed for the subsonic and transonic regime, schlieren imaging cannot be performed for these tests.

The Mach number range of the TMK is supplemented by the Hypersonic Wind Tunnel (H2K), where Mach numbers of up to  $Ma = 11.2$  can be tested. Due to compatible model adapters of the two wind tunnels, the same wind tunnel models can be used in both facilities. The facilities are described more in detail in Refs. [1] and [2].

Figure 2 shows the open test section of the TMK; the performance map of the facility is shown in Figure 3.

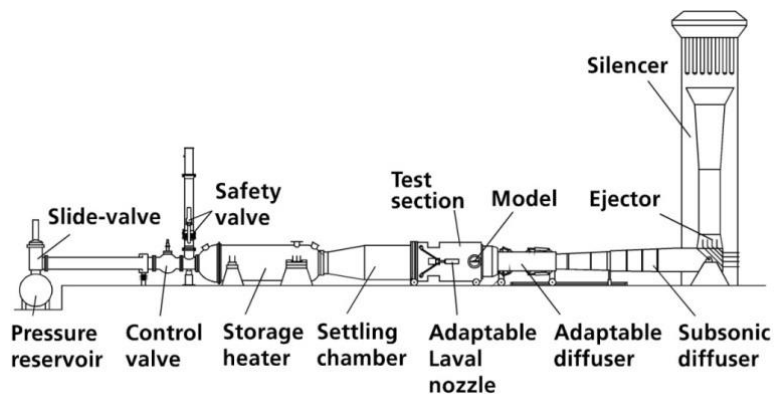


Figure 1: Schematic of Trisonic Wind Tunnel TMK

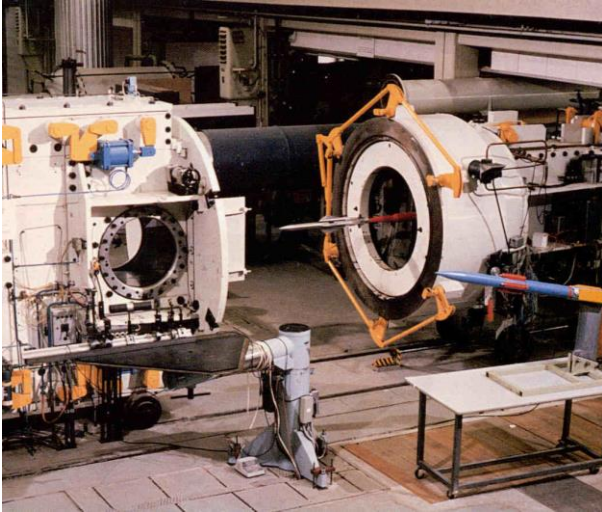


Figure 2: Supersonic test section of Trisonic Wind Tunnel TMK

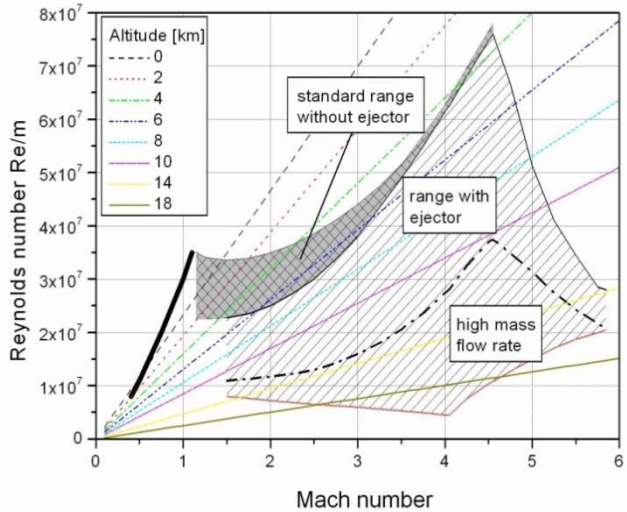


Figure 3: Performance map of Trisonic Wind Tunnel TMK

### 3. Wind Tunnel Model

#### 3.1 Tested Configurations

The primary goal of the project CALLISTO is the demonstration of a “toss-back” flight profile with the following flight phases [5]:

- Ascent phase (comparable to expendable launchers)
- “tilt-over”-maneuver
- “boost back” phase
- Aerodynamic guided approach phase
- Landing boost and touchdown

In this first series of wind tunnel experiments, the ballistic ascent phase and the aerodynamic guided approach of CALLISTO were investigated which are the FFN and the UFN configurations; these are shown in Table 1.



FFN (C1)		<u>Ballistic</u> MECO#1 – Fin Deploy	Folded	Folded	No Thrust Plume
UFN (C2)		<u>Ballistic:</u> Fin Deploy – MEIG#2 <i>and</i> <u>Aerodynamic Descent:</u> MECO#2 – MEIG#3	Unfolded (Deployed)	Folded	No Thrust Plume

Table 1: CALLISTO Configurations [5]

### 3.2 Reference Shape

The reference shape for the wind tunnel models was CAL1B as defined in Ref. [5]. It is the reference shape for the phase B which does not include protuberances like fuel lines, actuators etc.. The first version of the Aerodynamic Data Base (AEDB) was computed for this shape. Figure 4 shows the reference shape.

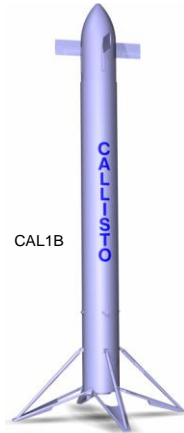


Figure 4: Reference shape CAL1B [5]

### 3.3 Model Scale and Design

Based on the reference shape a wind tunnel model was designed. The scaling was chosen to minimize blockage of the wind tunnel. The model is mounted on a biconical sting, which is then mounted on the motion control device of the  $\alpha$ -drive. A sketch of the wind tunnel model for the FFN and the UFN configuration mounted on the sting can be seen in Figure 5.

The model was designed in a modular manner. This way, the forward facing FFN configuration ( $\alpha = 0^\circ \dots 20^\circ$ ) and the backwards facing UFN configurations ( $\alpha = 180^\circ \dots 160^\circ$ ) can be tested with the same model. Furthermore, several deflection angles of the planar fins can be tested. The modules of the model are shown in Figure 6. The model mounted on the sting in the wind tunnel is shown in Figure 7. Note that the configuration shows a step in the diameter, due to the insulation of the tanks (see Figure 5 and Figure 7a).

The modules of the forward facing FFN configuration are: sleeve, center body, folded legs, complete nose for FFN, folded fins and a cover for the back part of the model. In this configuration the base of the model is open, as the sting is introduced in the model from this part (see Figure 7a). The backward facing UFN configuration consists of: sleeve, center body, folded legs, a cover representing the engine of the vehicle, unfolded fins and a cut nose. There are three versions of the module of the unfolded fins for the three deflection angles  $\delta = 0^\circ, 10^\circ, 20^\circ$ . In this configuration the sting is introduced from the nose in the model (see Figure 5b and Figure 7b).

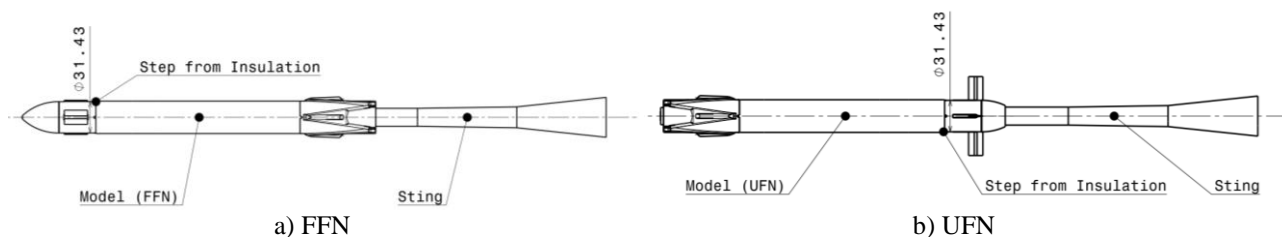


Figure 5: Dimensions of the Model for the FFN and the UFN configuration

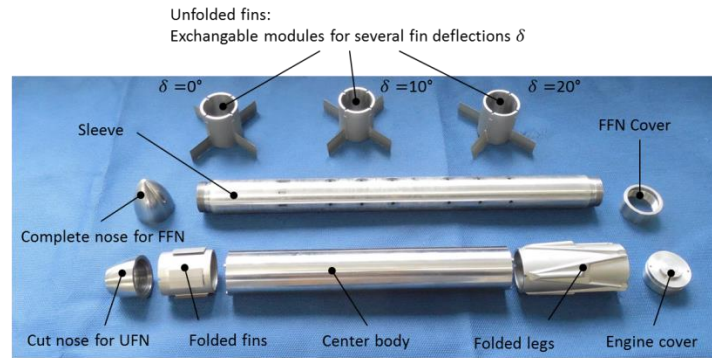


Figure 6: Modular Wind Tunnel Model



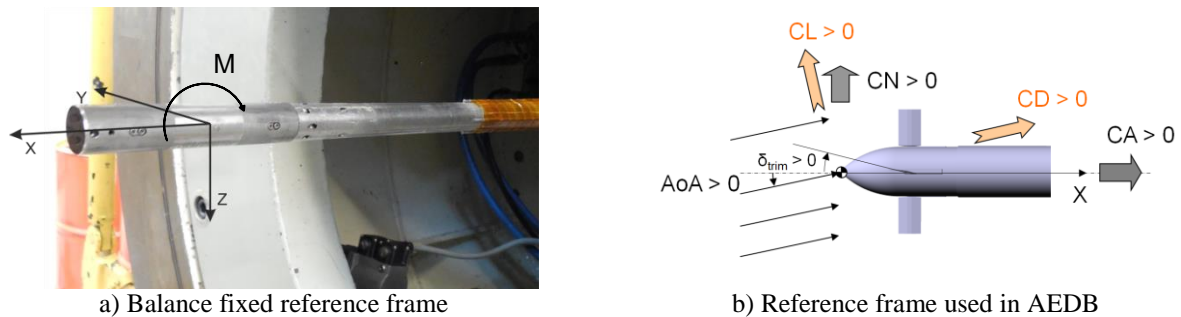
a) Forward facing FFN configuration

b) Backward facing UFN configuration

Figure 7: Model mounted in the Trisonic Wind Tunnel (TMK)

### 3.4 Reference Frame

The forces and moments were measured in a coordinate system fixed to the balance. It is shown in Figure 8a. However, in this report the data has been transformed to the coordinate system used in the Aerodynamic Data Base (AEDB), which is shown in Figure 8b. For comparable results in both reference frames, the origin of the balance fixed reference frame was positioned on the tip of the nose of the model. Hence, for the UFN configuration, due to its cut nose, the origin lies outside the model in an imaginary nose tip.

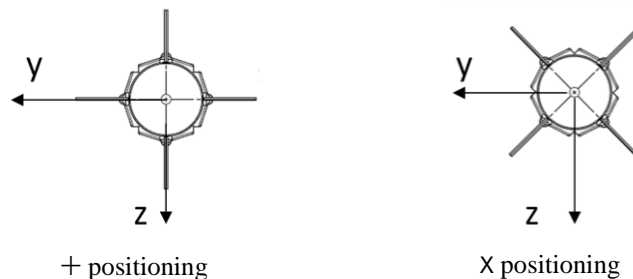


a) Balance fixed reference frame

b) Reference frame used in AEDB

Figure 8: Basis Fixed Coordinate System

The UFN configuration is investigated in a + and a X positioning. This refers to the position of the fins with respect to the angle of attack. In the + positioning the axis of rotation of the fins is parallel to the axis of the pitch rotation. In the X positioning the vehicle is turned 45° around the x axis in comparison with the + positioning. The X and the + position are sketched in Figure 9. In this paper only result for the + positioning are presented.



+ positioning

X positioning

Figure 9: Sketch of the + and X positioning of the vehicle

#### 4. Model Instrumentation

For the static force and moments measurements the model was equipped with a six component strain gauge floating frame balance *Task 0.75"*. This balance was selected as trade-off between the feasible axial load and the ratio of the model to sting diameter. The floating frame design leads to small contact areas of the balance and the model, which is why these balances yield high accuracies.

#### 5. Uncertainties

The uncertainties of the forces and moment measurements can be calculated from the measured input parameters via the error propagation by Gauss. For the supersonic tests the Mach number is determined by the contour of the nozzle, while for the transonic and subsonic tests it is controlled with the adaptable diffuser downstream of the test section. Therefore, the procedure for the calculation of the uncertainties varies for supersonic and transonic or subsonic tests.

The uncertainties of the following input parameters were taken into account in the calculation of the uncertainties of the forces and moment measurements: stagnation pressure, static pressure, Mach number, heat capacity ratio and the uncertainties in the force and moment measurements themselves.

#### 6. Test Procedure

A typical run of  $\alpha$  over the time is shown in Figure 10. First a slight down-sweep is performed to  $-3^\circ$ . This way, the following up-sweep runs with a constant sweep velocity of  $2^\circ/\text{s}$  while passing  $\alpha = 0^\circ$ . The up-sweep is performed up to a maximum angle of attack. In the position of maximum angle of attack the model is hold. Then, a down-sweep to  $0^\circ$  is performed. The data is evaluated for the main up- and the main down-sweep. In this way, hysteresis effects can be analyzed. The data is filtered with a 2 Hz low-pass filter in the post-processing.

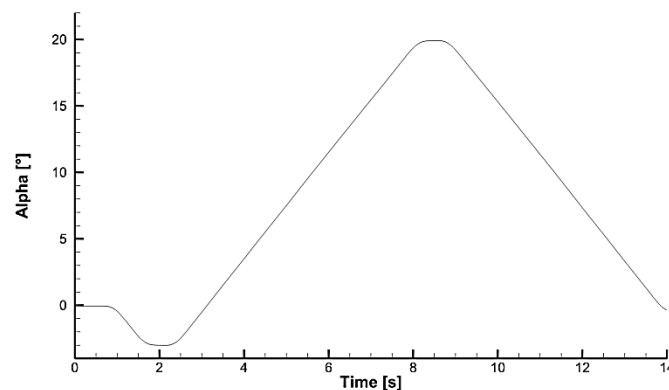


Figure 10: Typical  $\alpha$  over time

#### 7. CFD Computations with DLR Flow Solver TAU

The results of the wind tunnel experiments are compared to CFD computations for the AEDB which were computed with the DLR Navier-Stokes solver TAU with the Spalart-Almaras turbulence model. Computations were described more in detail in Ref. [5].

TAU is a flow solver developed by the DLR Institute of Aerodynamics and Flow Technology in Brunswick and Göttingen, Germany. It is capable of computing viscous and inviscid flows for subsonic up to hypersonic flow regimes around complex geometries on structured, unstructured and hybrid grids. Important flow features can be resolved with adaptive mesh refinement. [6][7]

The uncertainties of the CFD computations were estimated based on experience gained in previous projects.

## 8. Matrix of Performed Tests

Table 2 shows the configurations and flow conditions of the performed tests. The tests included subsonic up to supersonic flow conditions for the FFN and UFN configurations described in Table 1. The fin deflection angles of  $\delta = 0^\circ, +10^\circ, -10^\circ, +20^\circ, -20^\circ$  were tested. However, in this paper only results for  $\delta = 0^\circ$  (no fin deflection) are presented. The results of a variation of the deflection angles will be presented in follow-up papers [8][9].

Table 2: Matrix of performed tests

<b><i>Ma</i></b>	<b>Model</b>	<b>Defl. <math>\delta</math> [°]</b>	<b><i>Re</i> [1/m]</b>	<b><math>p_\infty</math> [bar]</b>	<b><math>T_\infty</math> [K]</b>	<b><math>q_\infty</math> [bar]</b>
<b>Mach number</b>	<b>Configuration</b>	<b>Fin deflection</b>	<b>Reynolds number</b>	<b>Static pressure</b>	<b>Temperature</b>	<b>Dynamic pressure</b>
0.50	FFN	-	1.44E+07	1.05	251.1	0.18
0.70	FFN	-	2.18E+07	1.07	239.5	0.37
0.90	FFN	-	3.01E+07	1.07	227.3	0.61
1.10	FFN	-	3.89E+07	1.10	223.4	0.93
1.50	FFN	-	3.30E+07	0.56	195.1	0.90
2.00	FFN	-	3.48E+07	0.34	160.0	0.96
2.50	FFN	-	3.71E+07	0.21	128.6	0.94
0.50	UFN	0	1.34E+07	1.07	267.6	0.19
0.70	UFN	0	2.00E+07	1.07	255.3	0.37
0.90	UFN	0	2.90E+07	1.07	233.2	0.60
1.12	UFN	0	3.81E+07	1.07	220.7	0.94
1.50	UFN	0	3.38E+07	0.57	193.4	0.91
2.00	UFN	0	3.62E+07	0.34	156.2	0.97
2.50	UFN	0	3.84E+07	0.22	126.0	0.94

For Mach number 1.1 and 0.9 the blockage of the wind tunnel can get critical. High loads occurred for the balance for Mach 1.1 for  $\alpha > 15^\circ$ . Therefore, for this Mach number the angle of attack was limited to  $15^\circ$  ( $165^\circ$  for UFN configurations). For most configurations for supersonic conditions, angles of attack of higher than  $20^\circ$  (less than  $160^\circ$  for UFN configurations) could be run. For consistency of the data base of the WTT data, it was limited to  $20^\circ$  for all cases except for the Mach 1.1 case which was limited to  $15^\circ$ .

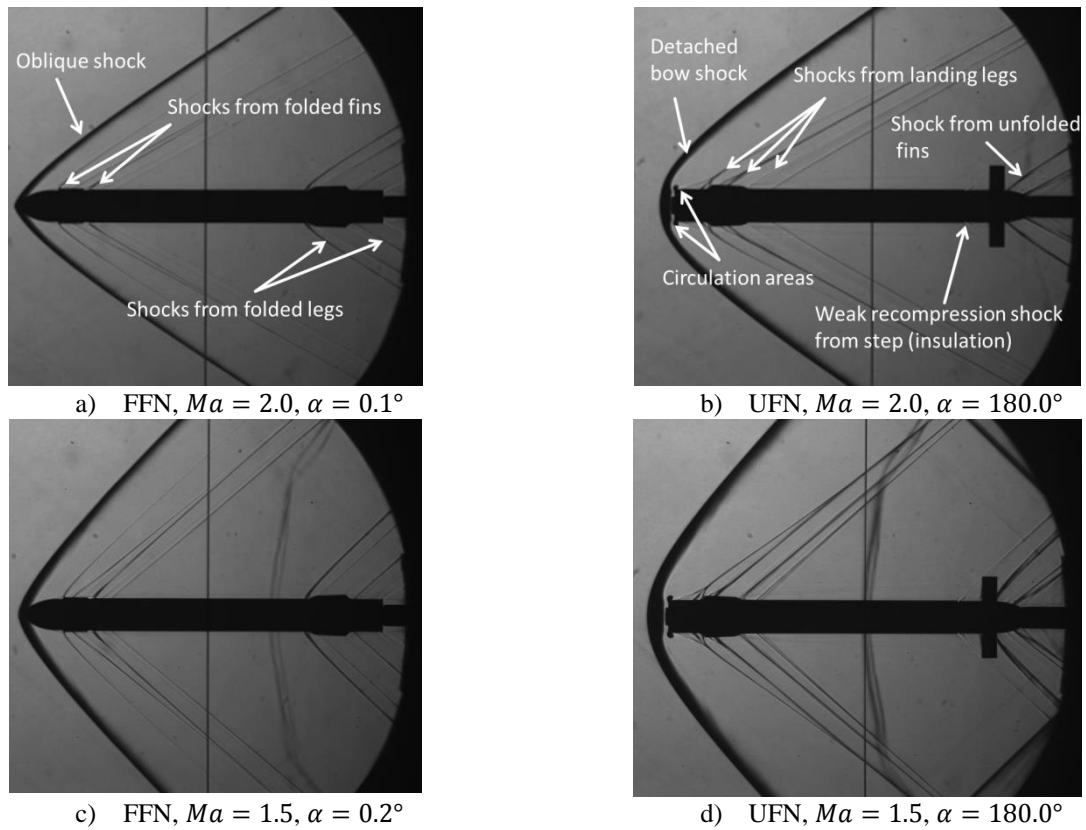
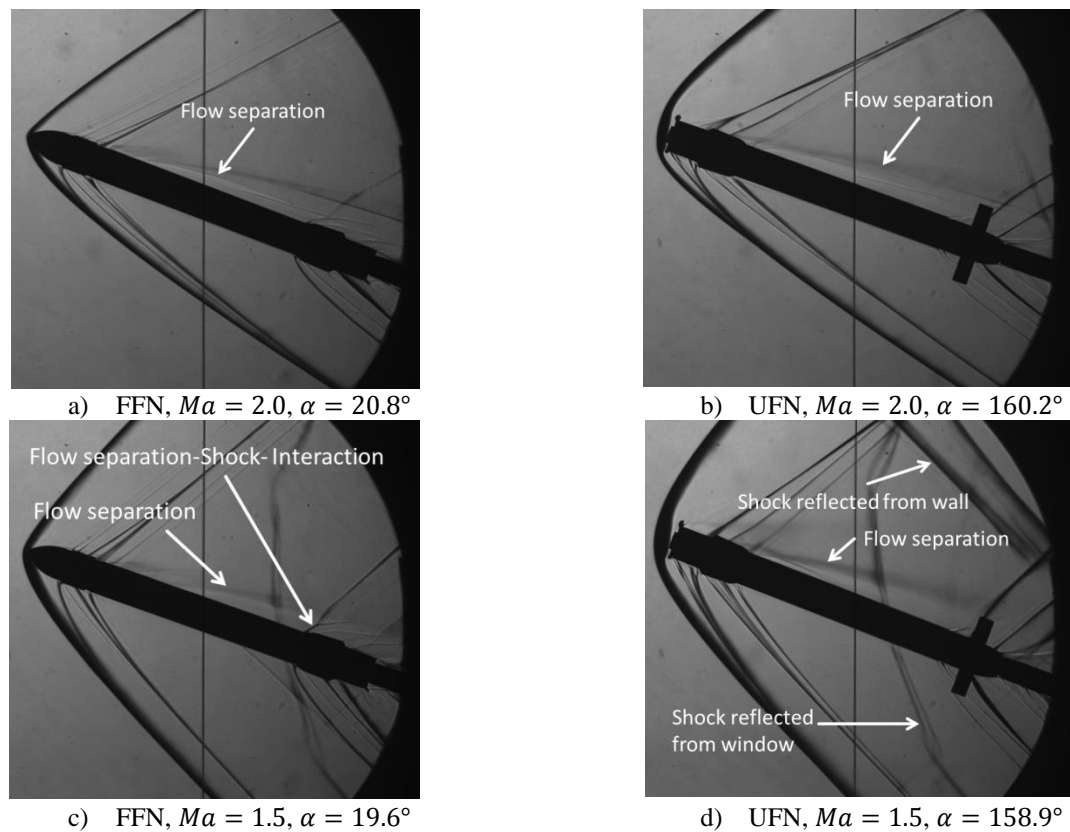
## 9. Test Results

### 9.1 Analysis of Flow Topology

In Figure 11 and Figure 12 schlieren images of the FFN and the UFN configuration are compared. For Mach 2.0 and  $\alpha = 0^\circ$  an oblique shock emerges from the tip of the vehicle for the FFN configuration (see Figure 11a). Shocks also emerge upstream of the folded fins and downstream of the fins after recompression. Also the landing legs lead to oblique shocks upstream of the legs and weaker recompression shocks downstream. The UFN configuration shows a detached bow shock in front of the backward facing base surface (Figure 11b). At its edge recirculation areas occur. Furthermore, weak shocks emerging from the edge of the base plane merge further downstream with the shock of the landing legs. Oblique shocks can also be observed at the fins. The step in the diameter of the center body due to the tank insulation only leads to relatively weak shocks in both configurations.

Figure 11c and Figure 11d show the FFN and the UFN configuration for Mach 1.5. The flow topology is similar to Mach 2.0. The shocks upstream of the folded fins and the folded legs and the recompression shocks downstream can be observed more precisely. Also the shock emerging from the unfolded fins can be observed.

Figure 12 shows the FFN configuration and the UFN configuration at angles of attack of  $\alpha = 20^\circ$  and  $\alpha = 160^\circ$  respectively. The leeward shocks become weaker while the windward shocks become stronger than for small angles of attack. For both configurations flow separation from the central body can be observed for these high angles of attack. Especially for the FFN configuration at Mach 1.5 an interaction of the flow separation with the shocks emerging from the landing legs can be observed. For Mach 1.5 the oblique shock at the tip of the FFN configuration and the bow shock upstream of the UFN configuration are reflected at the window of the wind tunnel. For Mach 1.5 and  $\alpha = 158.9^\circ$  for the UFN configuration also a reflection of the bow shock from the wind tunnel wall is visible in the schlieren image. However, the data is still valid as the shocks are not impinging on the model.

Figure 11: Comparison of schlieren images of the FFN and UFN at  $\alpha \approx 0^\circ$  and  $\alpha \approx 180^\circ$  respectivelyFigure 12: Comparison of schlieren images of the FFN and UFN at  $\alpha \approx 20^\circ$  and  $\alpha \approx 160^\circ$  respectively



## 9.2 Alpha Polars

In the following the detailed test results of the force and moment measurements are presented for the FFN configuration and for the UFN configuration with  $\delta = 0^\circ$ . They are compared to the CFD results from the AEDB. For the moment coefficient  $C_M$  based on the center of gravity (CoG), the position of the center of gravity was assumed as 60.00% of the length of the model from the nose tip of the model ( $x_{tip} = 0 \text{ mm}$ , see Figure 8b).

Also priorly estimated uncertainties for the CFD data in the AEDB are shown. The data of the wind tunnel experiments is shown with the uncertainties calculated as described in section 5. For a better comparison between the Mach numbers the scaling is kept equal for all Mach numbers for the aerodynamic coefficients.

No base pressure correction is implemented for CA as the model is not closed at the back side where the sting is introduced and hence the pressure inside the model can be assumed to be equal to the base pressure. Therefore, a pressure correction is not necessary.

As mentioned in section 2, schlieren windows cannot be installed in the transonic test section due to the perforated walls. Hence, schlieren images are only shown for the supersonic tests in the results.

Figure 13, Figure 14, Figure 15 and Figure 16 show the results for the ballistic ascent configuration FFN. Figure 13 shows that especially for the supersonic regime, the deviations of the CFD and the results of the Wind Tunnel Tests (WTT) are small. However, also for the lower supersonic, the transonic and the subsonic regime (see Figure 14, Figure 15 and Figure 16) the results of the WTT and the CFD computations show reasonable agreement and the deviations of the results of the WTT and the CFD computations are in the order of magnitude of the previously estimated uncertainties of the CFD. The uncertainties of the WTT are smallest for higher Mach numbers and getting larger for smaller Mach numbers.

Figure 17, Figure 19 and Figure 20 show the results for the ballistic descent configuration UFN. For UFN the deviations of CFD and WTT results are in the order of magnitude of the previously estimated uncertainties of the CFD. However single measurement points show larger discrepancies (e.g.  $C_M$  (CoG) at Mach 0.9 and  $\alpha = 160^\circ$ ). Therefore, the correct determination of the overall uncertainties of WTT and CFD and the merging of the data is still ongoing work.

Figure 17 to Figure 20 show, that  $C_M(\text{CoG})$  is positive for  $\alpha < 180^\circ$  and zero at  $\alpha = 180^\circ$  for all tested Mach numbers of the UFN configuration. Hence, the UFN configuration will return to  $\alpha = 180^\circ$  and is statically stable for the backward flight at the given center of gravity. The center of gravity at 60% of the vehicle length is a conservative assumption as, due to the fuel consumption, it will constantly move further backwards (moving away from the nose tip) during descent and therefore increase the stability of the backward flying configuration.

The deviation of CA is very small for all configurations and Mach numbers. This underpins the statement, that a pressure correction with the base pressure is not necessary. For all coefficients hysteresis effects are negligible.

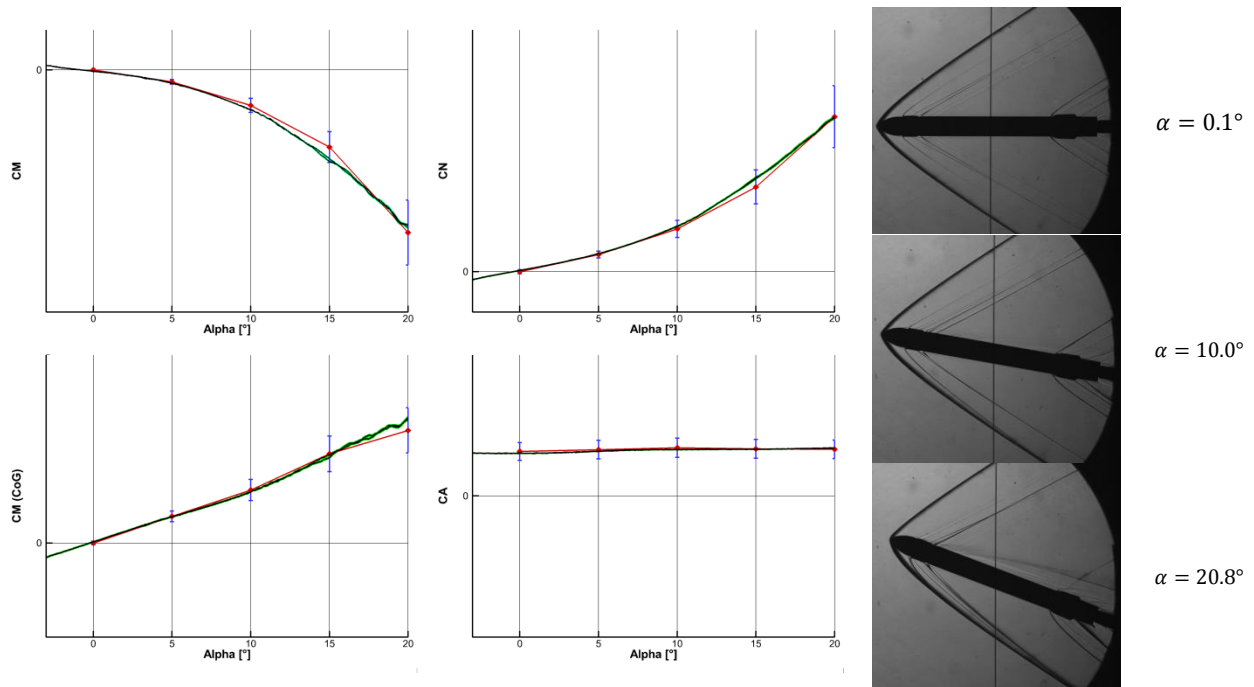


Figure 13: Left: Forces and Moments Coefficients for FFN, Mach 2.0 ( $\alpha < 20^\circ$ ); Red diamond – CFD in AEDB, blue error bars – estimated uncertainty for CFD results, black line – WTT results, green error bars – uncertainty of WTT results. Right: Schlieren images.

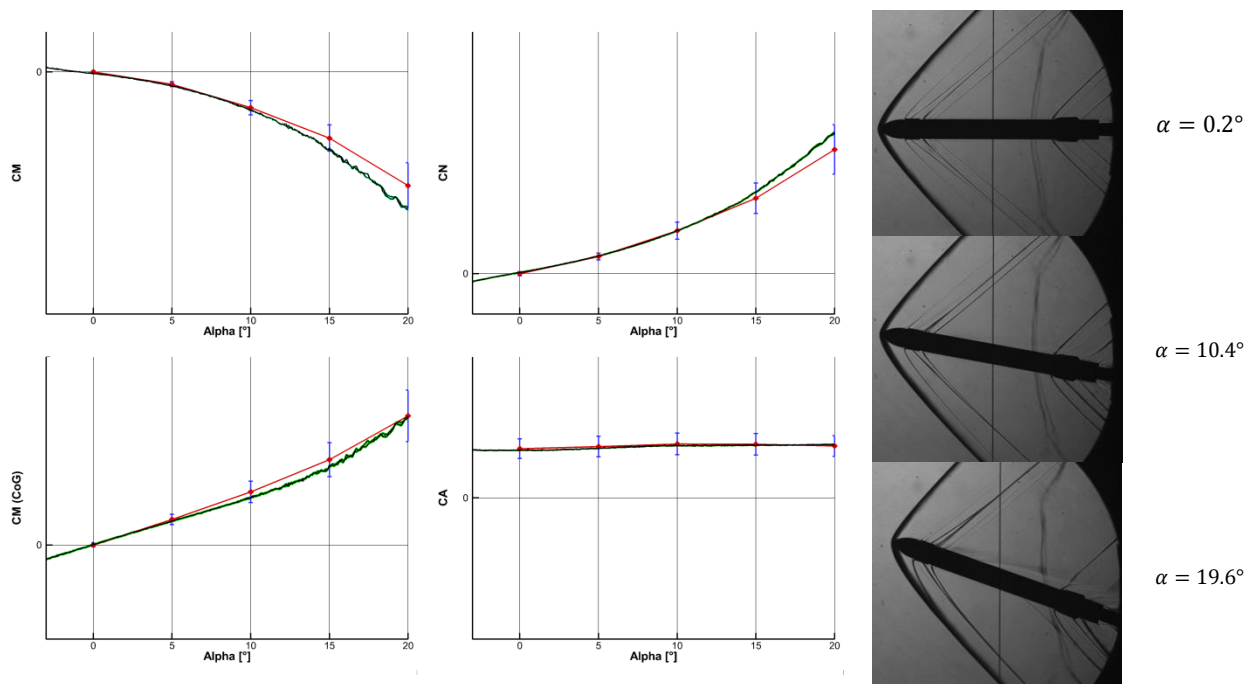


Figure 14: Forces and Moments Coefficients for FFN, Mach 1.5 ( $\alpha < 20^\circ$ ); Red diamond – CFD in AEDB, blue error bars – estimated uncertainty for CFD results, black line – WTT results, green error bars – uncertainty of WTT results. Right: Schlieren images.

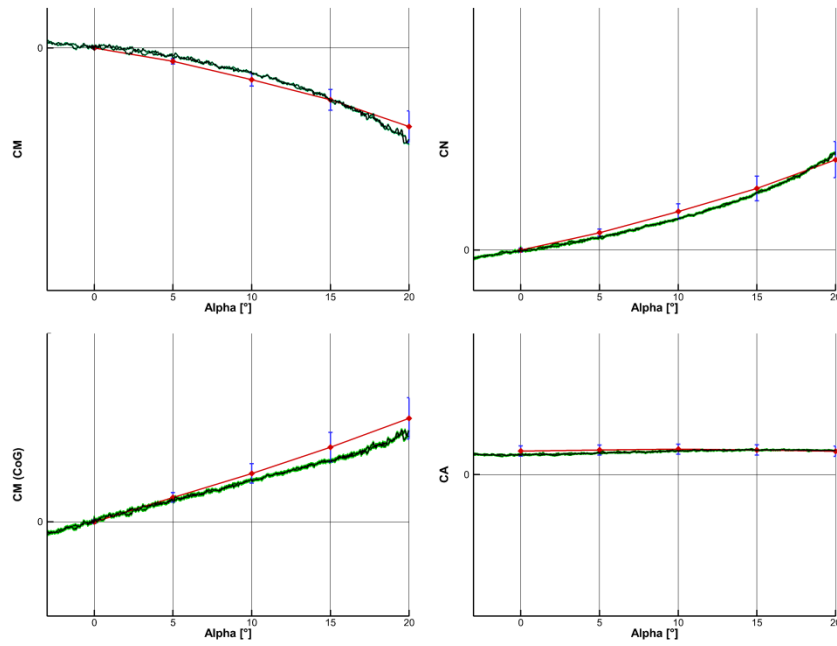


Figure 15: Forces and Moments Coefficients for FFN, Mach 0.9 ( $\alpha < 20^\circ$ ); Red diamond – CFD in AEDB, blue error bars – estimated uncertainty for CFD results, black line – WTT results, green error bars – uncertainty of WTT results.

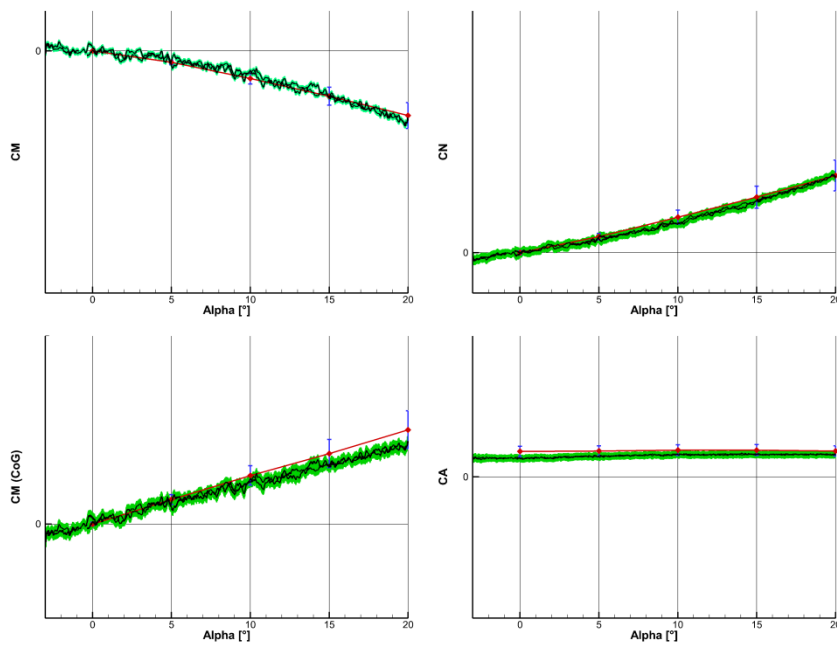


Figure 16: Forces and Moments Coefficients for FFN, Mach 0.5 ( $\alpha < 20^\circ$ ); Red diamond – CFD in AEDB, blue error bars – estimated uncertainty for CFD results, black line – WTT results, green error bars – uncertainty of WTT results.

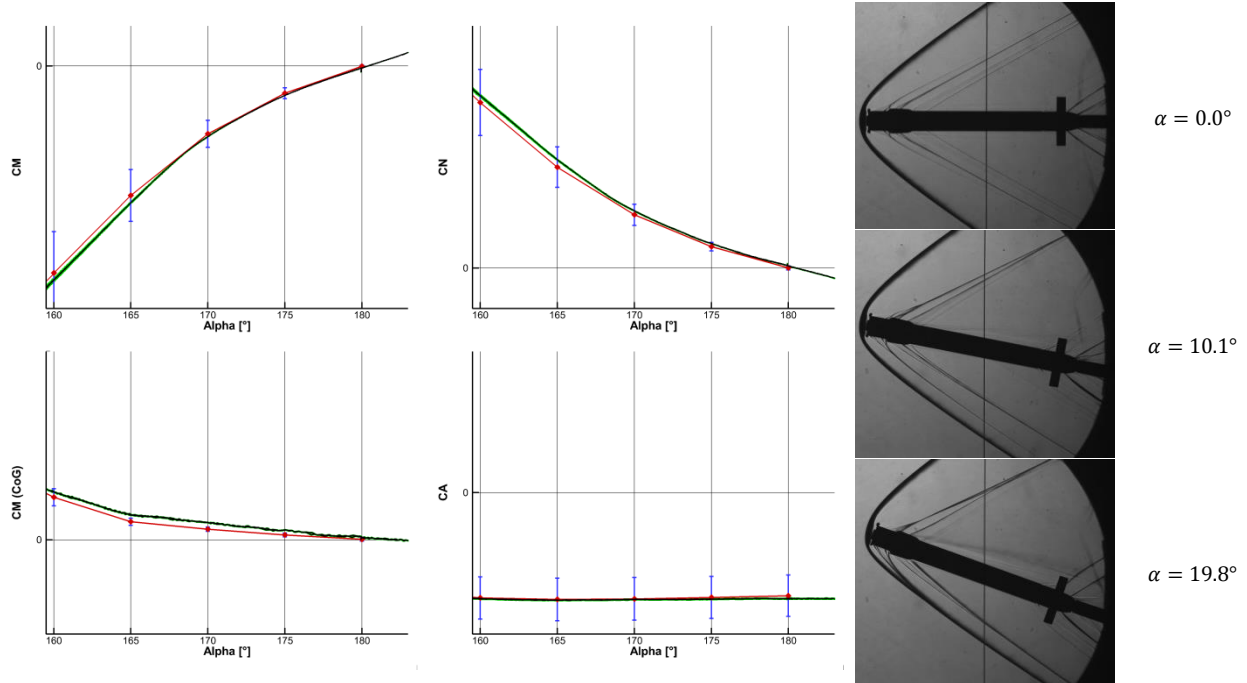


Figure 17: Forces and Moments Coefficients for UFN + 0, Mach 2.0 ( $\alpha > 160^\circ$ ); Red diamond – CFD in AEDB, blue error bars – estimated uncertainty for CFD results, black line – WTT results, green error bars – uncertainty of WTT results. Right: Schlieren images.

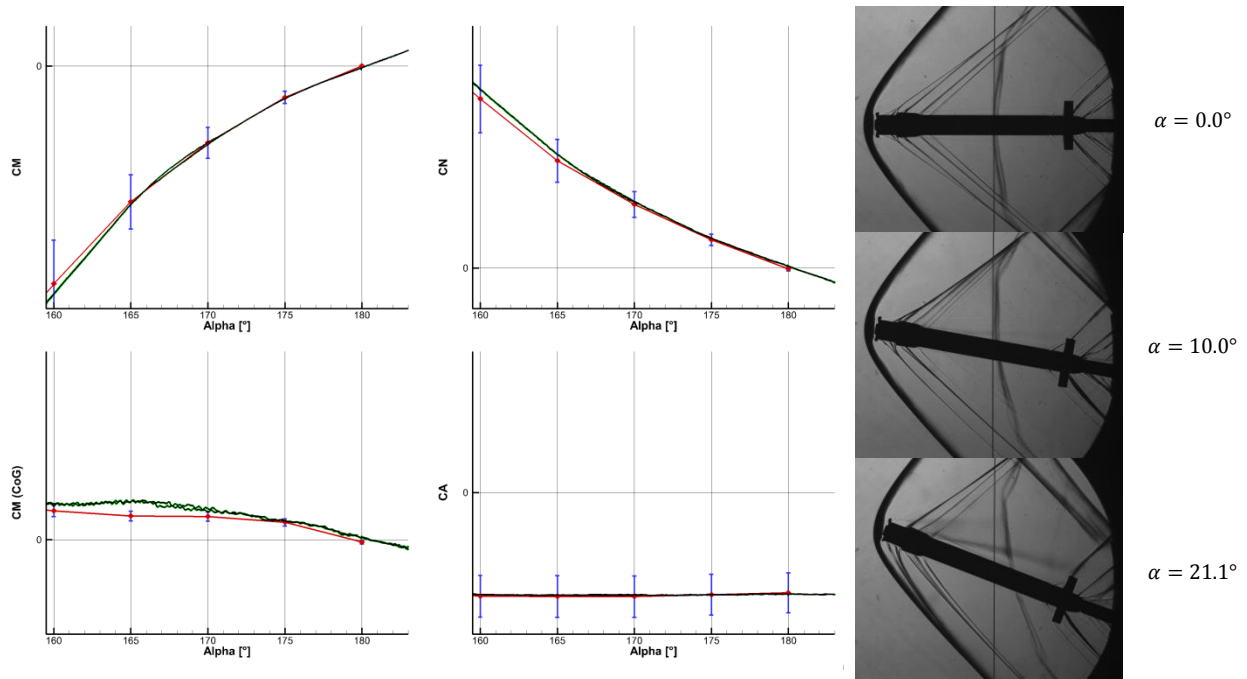


Figure 18: Forces and Moments Coefficients for UFN + 0, Mach 1.5 ( $\alpha > 160^\circ$ ); Red diamond – CFD in AEDB, blue error bars – estimated uncertainty for CFD results, black line – WTT results, green error bars – uncertainty of WTT results. Right: Schlieren images.

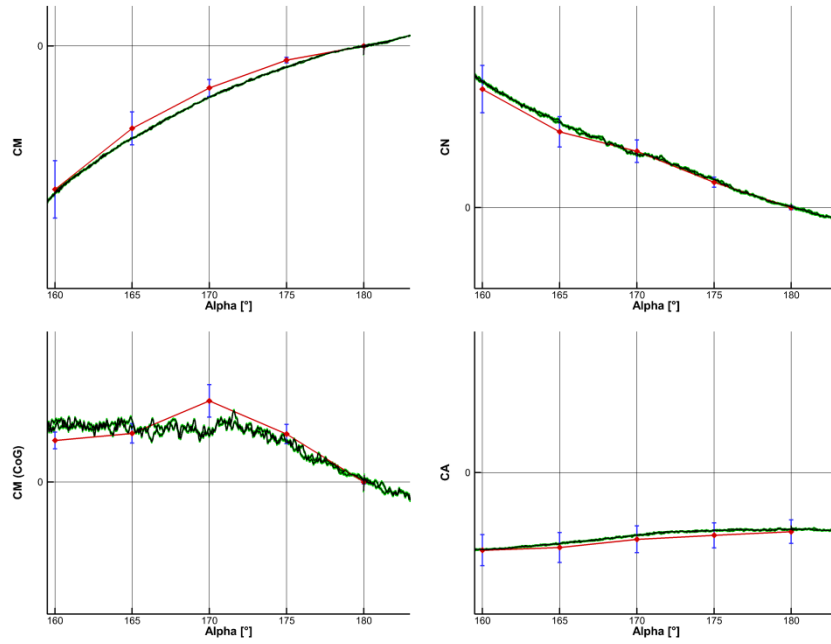


Figure 19: Forces and Moments Coefficients for UFN + 0, Mach 0.9 ( $\alpha > 160^\circ$ ); Red diamond – CFD in AEDB, blue error bars – estimated uncertainty for CFD results, black line – WTT results, green error bars – uncertainty of WTT results.

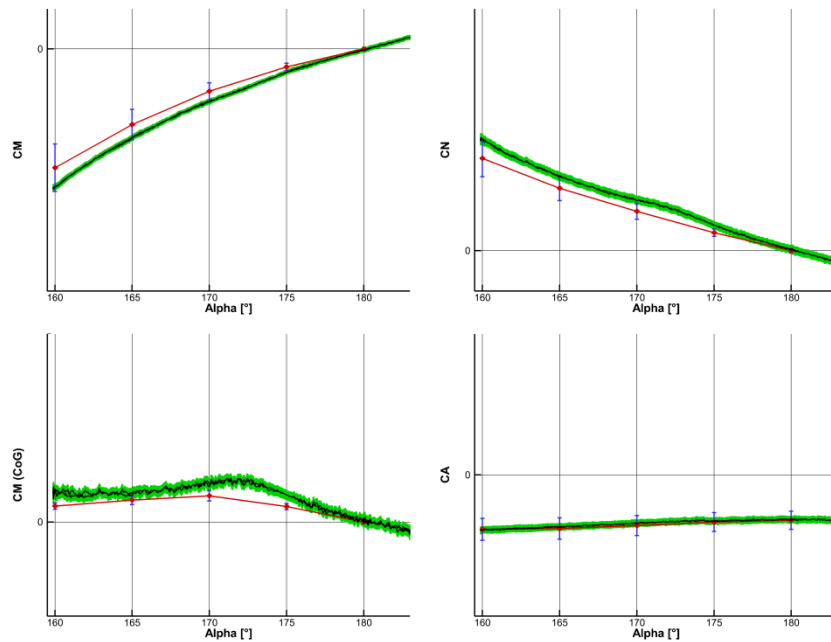


Figure 20: Forces and Moments Coefficients for UFN + 0, Mach 0.5; Red diamond – CFD in AEDB, blue error bars – estimated uncertainty for CFD results, black line – WTT results, green error bars – uncertainty of WTT results.

### 9.3 Mach Dependence of Lift and Drag

For the computation of trajectories, the evaluation of the drag coefficient (CD) the lift coefficient (CL) and the ratio of lift over drag L/D or CL/CD is important.

Figure 21 shows the dependence of the drag coefficient of the Mach number for an angle of attack of  $0^\circ$ ,  $10^\circ$  and  $15^\circ$  for the FFN configuration and of  $180^\circ$ ,  $160^\circ$  and  $165^\circ$  for the UNF configuration with  $\delta = 0^\circ$ . For the FFN configuration the drag coefficient stays relatively constant in the subsonic regime. In the transonic regime the drag coefficient rises; in the supersonic regime it falls slightly. The UNF represents a blunt body, therefore it shows different features. Due to the blunt forward facing base plane, the drag coefficient is higher for the UNF than for the FFN configuration. Already in the subsonic regime it rises with higher Mach numbers; in the supersonic regime it is relatively constant.

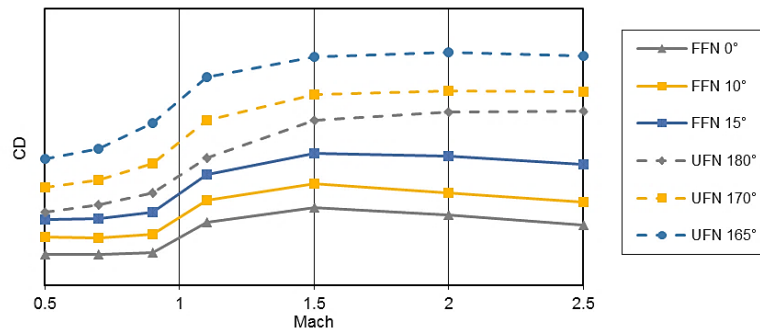


Figure 21: CD over Mach number for several angles of attack  $\alpha$

Figure 22 shows the dependence of the lift coefficient (CL) of the Mach number. For a better comparison for the UNF configuration  $-CL$  is plotted. As expected for both configurations the lift is higher for higher angles of attack. The UNF configuration shows higher lift due to the fins. However, for supersonic speeds higher than approx.  $M = 2.0$  the lift of the UNF configuration falls below the values of the FFN configuration.

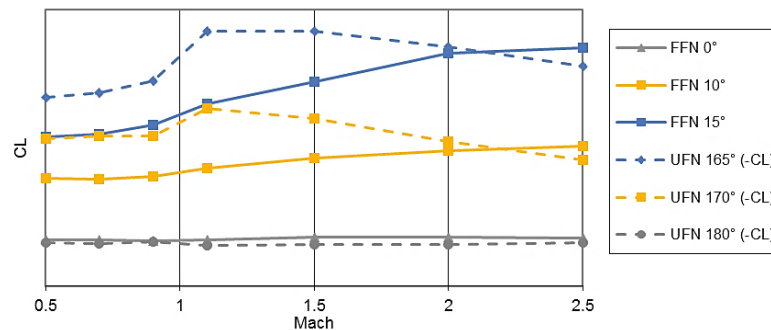


Figure 22: CL over Mach number for several angles of attack  $\alpha$

Figure 23 shows the lift over drag ratio of the two configurations. Also in this diagram  $-L/D$  is shown for the UNF configuration for the sake of a better comparability with the FFN configuration. The higher drag of the UNF configuration leads to a lower L/D for all Mach numbers for the UNF configuration even though the Lift is higher for  $M \leq 2.0$ .

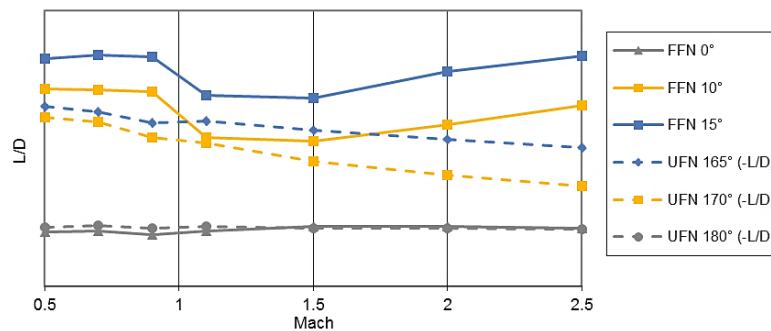


Figure 23: L/D over Mach number for several angles of attack  $\alpha$

## 10. Conclusion

Wind tunnel tests have been carried out with a model of the CALLISTO demonstrator reference shape CAL1B. Schlieren visualization gave insight in the flow topology for supersonic Mach numbers. However, for a better understanding of the flow topology and for visualization in the transonic and subsonic flow regime, oil flow pictures will be presented in follow-up papers [8][9].

The overall agreement of the force and moment coefficients of the CFD and the WTT results is good. The deviation between the CFD and WTT results are especially good for supersonic Mach numbers. For low supersonic, transonic and subsonic Mach numbers the deviations are of the same order of magnitude as the previously estimated uncertainties of the CFD results.

The drag coefficient is significantly higher for the UNF configuration than for the FFN configuration due to its blunt forward facing surface. Also the lift is higher for the UNF configuration due to its unfolded fins. The lift over drag ratio is smaller for UNF than for the FFN configuration.

For a complete understanding of the aerodynamic characteristics of the vehicle, the roll moment generated by a deflection of  $\delta = 10^\circ$  for all fins will be investigated [8]. Further wind tunnel tests are foreseen, to investigate the influence of protuberances (e.g. fuel lines, cable ducts) on the aerodynamic properties of the vehicle and cold gas experiments will be performed to model the effect of the plume.

## 11. Acknowledgements

The authors gratefully acknowledge the technical staff of the Trisonic Wind Tunnel (TMK), Martin Achner and Daniel Habegger, for their support and technical expertise.

## 12. References

- [1] Esch, H. 1986. Die 0.6-m x 0.6-m – Trisonische Meßstrecke (TMK) der DFVLR in Köln-Porz (Stand 1986). DFVLR-Mitt. 86-21, Cologne.
- [2] Niezgodka, F.-J. 2001. Der Hyperschallwindkanal H2K des DLR in Köln-Porz (Stand 2000). DLR-Mitt. 2001-01, Cologne.
- [3] Dumont, E., Ecker, T., Chavagnac, C., Witte, L., Windelberg, J., Klevanski, J., Giagkozoglou, S. 2018. CALLISTO – Reusable VTVL launcher first stage demonstrator. SP2018\_00406. In: *Space Propulsion Conference 2018*.
- [4] Tatioussian, P., Desmarioux, J., Garcia, M. 2017. CALLISTO Project - Reusable first stage Rocket Demonstrator, In: *7th European Conference for Aeronautics and Space Sciences*, Milano, Italy. DOI: 10.13009/EUCASS2017-680
- [5] Klevanski, J., Ecker, T., Riehmer, J., Reimann, B., Dumont, E., Chavagnac C. 2018. Aerodynamic Studies in Preparation for CALLISTO - Reusable VTVL Launcher First Stage Demonstrator. In: *69th International Astronautical Congress (IAC)*, IAC-18- D2.6.3, Bremen, Germany.
- [6] Schwamborn, D., Gerhold, T., and Heinrich, R. 2006. The DLR TAU-Code: Recent Applications in Research and Industry. In: *ECCOMAS CFD 2006 Conference*, TU Delft, Delft, The Netherlands.
- [7] Langer, S., Schwöppe, A., and Kroll, N. 2014. The DLR Flow Solver TAU—Status and Recent Algorithmic Developments. In: *52nd Aerospace Sciences Meeting*, AIAA Paper 2014-0080. doi:10.2514/6.2014-0080
- [8] Riehmer, J., Marwege, A., Klevanski, J., Gülhan, A., Dumont, E. 2019. Subsonic and Supersonic Ground Experiments for the CALLISTO VTVL Launcher Demonstrator. Accepted for: *International Conference on Flight Vehicles, Aerothermodynamics and Re-entry Missions and Engineering (FAR) 2019*, Milano, Italy.
- [9] Marwege, A., Riehmer, J., Klevanski, J., Gülhan, A., Dumont, E. 2019. Wind Tunnel investigations in CALLISTO - Reusable VTVL Launcher First Stage Demonstrator. Accepted for: *70th International Astronautical Congress (IAC)*. Washington, D.C., USA.